Surface magnon spectra of nodal loop semimetals

Assem Alassaf [*]
Department of Physics of Complex Systems, ELTE Eötvös Loránd University, Pázmány Péter sétány 1/A, 1117 Budapest, Hungary

János Koltai
Department of Biological Physics, ELTE Eötvös Loránd University, Pázmány Péter sétány 1/A, 1117 Budapest, Hungary

László Oroszlány
Department of Physics of Complex Systems, ELTE Eötvös Loránd University, Pázmány Péter sétány 1/A, 1117 Budapest, Hungary and Wigner Research Centre for Physics, Konkoly-Thege M. út 29-33, H-1121 Budapest, Hungary

(Received 27 July 2023; revised 4 November 2023; accepted 11 January 2024; published 26 January 2024)

In this paper, we establish a connection between the bulk topological structure and the magnetic properties of drumhead surface states of nodal loop semimetals. We identify the magnetic characteristics of the surface states and compute the system's magnon spectrum by treating electron-electron interactions on a mean-field level. We draw attention to a subtle connection between a Lifshitz-like transition of the surface states driven by mechanical distortions and the magnetic characteristics of the system. Our findings may be experimentally verified, e.g., by spin-polarized electron energy loss spectroscopy of nodal semimetal surfaces.

DOI: 10.1103/PhysRevB.109.035161

I. INTRODUCTION

Due to their unique electronic properties and potential applications in numerous fields, topological materials have attracted significant attention [1–6]. These materials possess nontrivial topological properties that in some cases need be protected by symmetries, resulting in the existence of robust surface or edge states. Topological semimetals are a class of topological materials that have been extensively studied in recent years [7,8]. Weyl and nodal line semimetals are two types of topological semimetals that possess distinct surface states. Weyl semimetals are distinguished by the presence of Weyl nodes in the bulk band structure, resulting in Fermi arcs on the surface [7,9]. These Fermi arcs connect the Weyl node projections and exhibit a variety of fascinating transport properties. Compared to Weyl semimetals, the stability of a nodal line generally requires a discrete symmetry [10]. Nodal line semimetals have been predicted to be present in realistic materials through the help of *ab initio* calculations [11]. In these calculations, however, it was highlighted that in materials where spin-orbit coupling is considerable, nodal lines, in general, are transformed into Dirac points. Recently a host of other materials have been proposed to host nodal loops [6]. In particular, Ca_3P_2 [12], a material where spin-orbit coupling is negligible, hosts a remarkably large nodal loop. The generalization of nodal semimetals to two-dimensional systems [13] and to knotted nodal topologies have also been studied [14]. The interest in nodal line semimetals continues to fuel theoretical and experimental results. The effect of disorder on the bulk [15] and on the surface state [16] was recently elucidated. Studies of magnetotransport properties of nodal line semimetals highlighted the connection between the Lorentz force and the planar magneto Hall effect [17], and stressed the importance of magnetic field-induced flat bands on nonlinear transport properties [18]. The observation of spin-polarized surface states in $SnTaS_2$ samples was reported recently [19]. Boosting of the thermoelectric effect in thin films of nodal line semimetals was proposed [20]. Theoretical aspects of the tunability of the topology of the nodal line itself were also investigated [21].

Engineering surface and interface magnetism has already had a tremendous impact on consumer electronics. The giant magnetoresistance effect underpins a host of data storage solutions to this day [22]. Exploiting spintronics architectures incorporating magnetic boundaries promises the realization of smaller, faster, and more energy efficient classical and quantum devices [23]. Surface magnetism in topological materials is an intriguing research direction offering opportunities to realize exotic quantum states of matter. For instance, gapping topological surface states by magnetism is a necessary ingredient in proposals for realizing Majorana modes [24]. Nodal loop semimetals, just as other topological insulators and semimetals, have characteristic surface states.

The drumhead states on the surfaces of nodal semimetals are dispersionless states associated with the surface projection of the nodal line structure. Due to their small kinetic energy, these drumhead states are susceptible to interactions and thus they can be an ideal platform for superconductivity [25,26] or emergent surface magnetism [8,27]. Rhombohedral graphite is a prime example of such a material whose interaction-induced magnetic properties have already been studied theoretically [28,29] and observed experimentally [30,31]. Exploring the impact of interactions on

[*]assem.al.assaf.abd.alrham@ttk.elte.hu

drumhead states further may unlock similar exciting applications as it has for their counterparts in other topological materials.

In this paper, we investigate a yet unexplored aspect of nodal loop semimetals, namely, the surface magnon spectrum. In systems where interactions induce magnetism on the surface, the magnon spectrum yields crucial experimentally accessible information regarding the surface states and indirectly about the bulk topological properties of the system as well. We shall focus on a generic description of observable phenomena associated with the magnon spectrum in our paper. Therefore, we will not use a material-specific model but rather a simple generic minimal model able to capture the most important aspects of the considered effects. Our findings should be relevant for experimental characterization of topological flat bands arising in nodal semimetals, especially when the flat bands extend over a considerable portion of the projected Brillouin zone, for example, as those in Ca_3P_2 [12,32].

In the next section, we introduce our model and describe the connection between the bulk nodal loop and drumhead surface states. Treating electron-electron interaction on a mean-field level, we obtain the magnetic properties of the surface states. Mapping to an isotropic Heisenberg spin model, we calculate the magnon spectrum of the system. We highlight a nuanced connection between the connectivity of the topological flat band and the magnon energies.

II. THE MODEL

In this section, we introduce the investigated model and describe the real-space structure and momentum space spectrum. The presence of a nodal loop, which is a closed curve in momentum space, is the key feature of our model. As we show, the shape of the nodal loop and the flat surface states stabilized by its presence can be controlled by a parameter that corresponds to mechanical distortion in an experimental setting.

A. Real-space structure

We consider a three-dimensional cubic system, spanned by the mutually perpendicular lattice vectors $\mathbf{a}_i$ of length a, with two sublattices (A and B). The real-space structure is depicted in Fig. 1(a). We take a single spinful orbital degree of freedom on each site into account. Electrons are allowed to hop from one site to the other without breaking the sublattice symmetry characterized by the real-space Hamiltonian:

$$\begin{aligned}\hat{H}_0 = \sum_{\mathbf{r},s} & \delta\xi t \hat{a}^\dagger_{\mathbf{r},s}\hat{b}_{\mathbf{r},s} - 2\xi t \hat{a}^\dagger_{\mathbf{r},s}\hat{b}_{\mathbf{r}+\mathbf{a}_3,s} \\ & - t\hat{a}^\dagger_{\mathbf{r},s}\hat{b}_{\mathbf{r}+\mathbf{a}_1,s} - t\hat{a}^\dagger_{\mathbf{r}+\mathbf{a}_1,s}\hat{b}_{\mathbf{r},s} \\ & - t\hat{a}^\dagger_{\mathbf{r},s}\hat{b}_{\mathbf{r}+\mathbf{a}_2,s} - t\hat{a}^\dagger_{\mathbf{r}+\mathbf{a}_2,s}\hat{b}_{\mathbf{r},s} + \text{H.c.}, \end{aligned} \tag{1}$$

where $\mathbf{r}$ represents a unit cell of the system, while s is the spin degree of freedom. The annihilation operator $\hat{a}_{\mathbf{r},s}$ acts on sublattice A and spin projection s, $\hat{b}_{\mathbf{r},s}$ acts on sublattice B. The hopping amplitude t controls the strength of electron movement between neighboring lattice sites and serves as the unit of energy for our model. The sublattice symmetry is the fundamental symmetry of the system which allows for the emergence of the nodal loop. The first term describes intra unit cell hopping between the two sublattices, the second term is a hopping in the perpendicular $\mathbf{a}_3$ direction. These two intra and inter unit cell hopping terms exhibit the same structure as the one-dimensional Su–Schrieffer–Heeger (SSH) model [33]. The remaining terms correspond to lateral hoppings between unit cells along the $\mathbf{a}_1$ and $\mathbf{a}_2$ directions. There are two important dimensionless parameters in the considered system δ and ξ. These parameters, as we will illustrate in the following subsection, control the shape and size of the nodal loop and the drumhead surface states. The parameter δ, governing the relative strength of intra- and intercell hopping along the $\mathbf{a}_3$ direction serves as an internal parameter that mimics a material-specific property of the system such as particular matrix elements of the Hamiltonian related to hopping from one orbital to the other. ξ, multiplies all hopping amplitudes in the $\mathbf{a}_3$ direction, and thus captures the effects of applying a uniaxial mechanical pressure on the system. The parameter ξ thus represents an experimentally tunable property. We note that in real materials, uniaxial strain connects distortions parallel and perpendicular to the strain axis. Thus, a more realistic description would include additional dimensionless parameters in the lateral directions as well. Considering these distortions, however, would unduly proliferate the parameters of the model without qualitatively impacting the presented conclusions. As we shall see below, both parameters δ and ξ have a significant impact on the electronic structure and magnetic properties of the system.

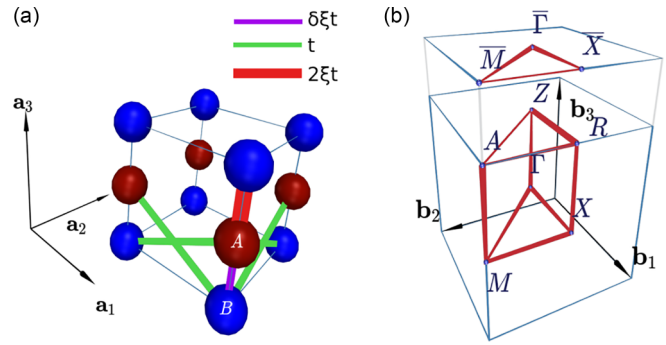

FIG. 1. Real-space structure (a) of the considered model. The two atoms in the unit cell, A and B, are coupled through three types of hopping procedures. In the lateral direction, spanned by $\mathbf{a}_1$ and $\mathbf{a}_2$, a sublattice altering hopping with strength t (denoted by green lines) is taken into account. In the perpendicular direction, defined by $\mathbf{a}_3$, there is a sublattice altering intra unit cell hopping with magnitude $\delta\xi t$ (denoted by purple line) and a sublattice altering inter unit cell hopping with magnitude $2\xi t$ (denoted by a thick red line) assumed. Momentum space and high symmetry points in the full and projected Brillouin zone (b) of the considered model.

B. Momentum space structure

As the investigated system is cubic, the corresponding Brillouin zone spanned by reciprocal lattice vectors $\mathbf{b}_i$ will also be cubic, as depicted in Fig. 1(b). As we will connect the topological properties of the bulk to the surface magnetic properties of a slab with finite thickness, it is instructive to introduce the projected Brillouin zone with its appropriate high-symmetry

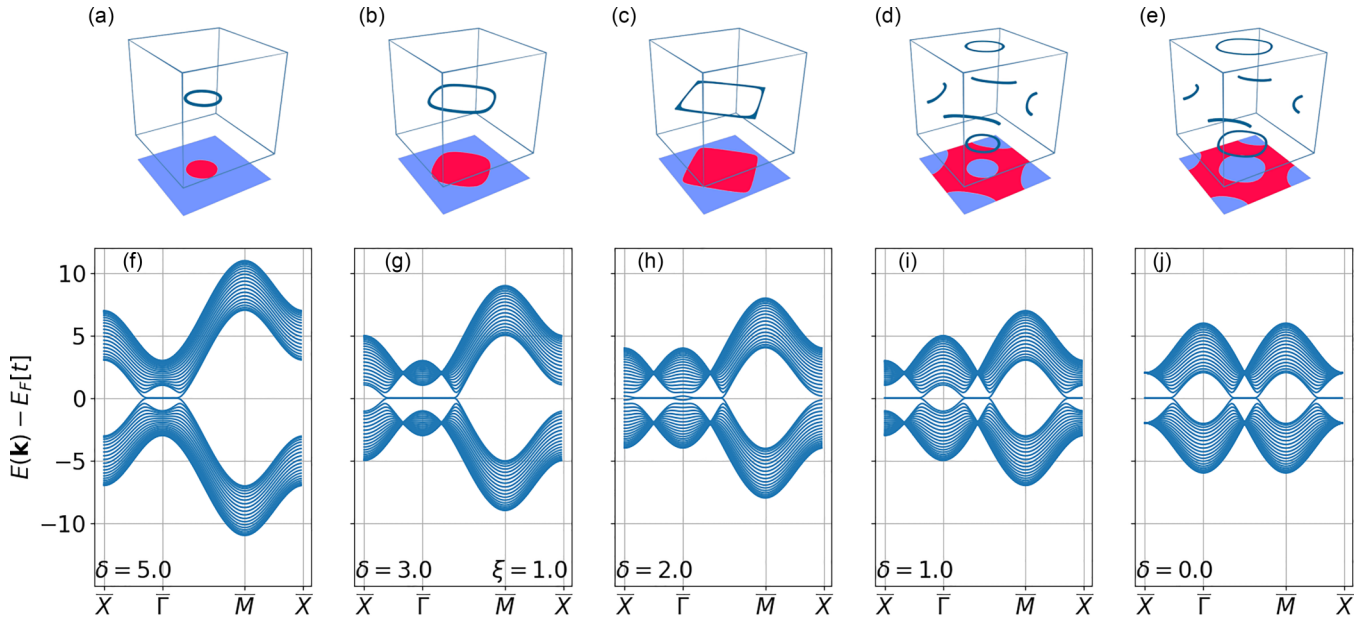

FIG. 2. The geometry of the nodal loop in the three-dimensional Brillouin zone and the winding number map in the projected Brillouin zone for various values of δ [(a)–(e)]. Purple shades in the lower plane correspond to winding number $\nu = 0$ while red signals $\nu = 1$. The band structure of a finite slab with a thickness of 20 unit cells was evaluated on a high symmetry path in the projected Brillouin zone for the same values of δ as above [(f)-(j)]. In all cases $\xi = 1.0$.

points, as shown in the figure too. To elucidate the momentum space structure defined by the kinetic Hamiltonian Eq. (1), we employ Fourier-transformed operators defined in the usual manner as

$$\hat{a}_{\mathbf{k},s} = \sum_{\mathbf{r}} e^{i\mathbf{k}\mathbf{r}} \hat{a}_{\mathbf{r},s}, \quad \hat{b}_{\mathbf{k},s} = \sum_{\mathbf{r}} e^{i\mathbf{k}\mathbf{r}} \hat{b}_{\mathbf{r},s}, \tag{2}$$

where $\mathbf{k} = k_x\mathbf{b}_1 + k_y\mathbf{b}_2 + k_z\mathbf{b}_3$ is a wave vector indexing states in the three-dimensional Brillouin zone. With these, we can recast Eq. (1) in a form that is diagonal in $\mathbf{k}$ as

$$\hat{H}_0 = \sum_{\mathbf{k},s} (\hat{a}^\dagger_{\mathbf{k},s}\ \hat{b}^\dagger_{\mathbf{k},s}) \mathcal{H}(\mathbf{k}) \begin{pmatrix} \hat{a}_{\mathbf{k},s} \\ \hat{b}_{\mathbf{k},s} \end{pmatrix}. \tag{3}$$

Here the matrix elements of $\mathcal{H}(\mathbf{k})$ are obtained by collecting terms after performing Fourier transformation, yielding

$$\begin{aligned} \mathcal{H}(\mathbf{k}) &= \left[\delta t_z - 2 \sum_{i=(x,y,z)} t_i \cos k_i \right] \sigma_x - 2t_z \sin k_z \sigma_y \\ &= \mathbf{d}_{\delta,\xi}(\mathbf{k}) \cdot \boldsymbol{\sigma}, \end{aligned} \tag{4}$$

with $t_{x,y} = t$, $t_z = \xi t$, and $\sigma_{x,y}$ are Pauli matrices acting on the sublattice space. We give further detail regarding the derivation of $\mathcal{H}(\mathbf{k})$ in Appendix A. The absence of σ_z from the above expression is the fingerprint of the sublattice symmetry of the model. Three-dimensional Hamiltonians with sublattice symmetry can be characterized by a winding number [34–36] associated to the $\mathbf{d}_{\delta,xi}(\mathbf{k})$ vector for specific paths in momentum space. The system for a given value of k_x and k_y mimics the behavior of the SSH model [33]. We calculate this winding number along k_z as we cross the Brillouin zone. For a given value of k_x, k_y, δ, and ξ, the winding number is evaluated as

$$\nu(k_x, k_y, \delta, \xi) = \begin{cases} 1 & |C_{\delta,\xi}(k_x, k_y)/2\xi t| < 1 \\ 0 & |C_{\delta,\xi}(k_x, k_y)/2\xi t| > 1, \end{cases} \tag{5}$$

where we introduce the shorthand $C_{\delta,\xi}(k_x, k_y) = \delta\xi t - 2t\cos k_x - 2t\cos k_y$. The winding number, which is a bulk property, signals the presence or absence of topological drumhead states for slabs. This is a manifestation of the bulk boundary correspondence [37]. If the winding number is nonzero for a given set of bulk parameters δ and ξ and wave vector components k_x and k_y, then in a slab geometry there will be a zero-energy surface state present at the corresponding wave vector.

The geometry of the nodal loop, the map of winding number, and the spectrum of a slab of a finite thickness can be observed for different values of δ but fixed values of ξ in Fig. 2, while in Fig. 3 the same is depicted but for fixed values of δ and changing ξ.

Let us discuss the evolution of the nodal loop and the drumhead states associated with it as the function of the parameters δ and ξ.

First, focusing on Fig. 2, that is, keeping $\xi = 1.0$, we can observe that, as one decreases δ, a nodal loop first appears at the Γ point of the bulk Brillouin zone, then grows in size. At $\delta = 2.0$, two drastic changes occur. First, the nodal loop around the Γ point is enlarged to a point where it coalesces with nodal loops from the neighboring Brillouin zone effectively transforming itself from a loop around Γ to a loop around M. Second, an additional nodal loop is germinated at the Z point of the bulk Brillouin zone due to a band crossing. The appearance and evolution of the nodal loops leave an impression on the winding number maps as well. For larger values of δ, where only a single loop is present, the region

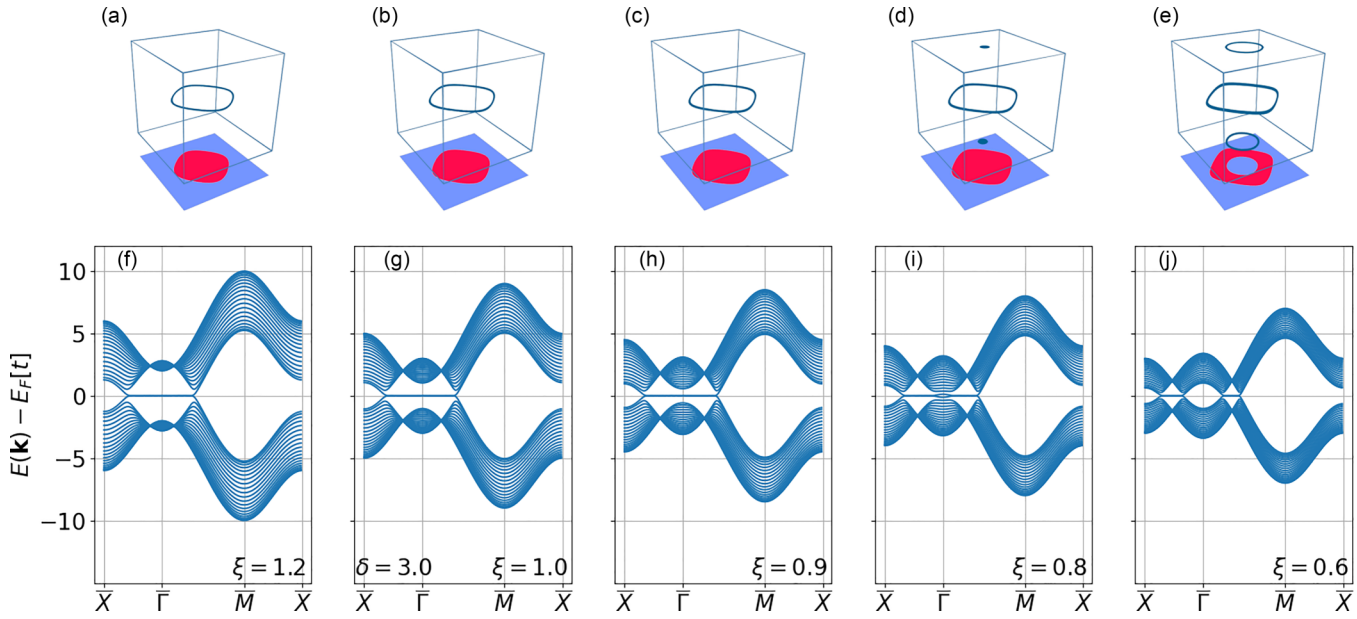

FIG. 3. The geometry of the nodal loop in the three-dimensional Brillouin zone, winding number map, and slab band structures as above for a fixed value of $\delta = 3.0$ and various values of ξ.

with $\nu = 1$ is a simply connected region in the shadow of the nodal loop. For $\delta < 2.0$, however, the appearance of the second loop and the coalescence of the original loop causes a drastic change in the connectivity of the region with a finite winding number, changing a simply connected region into a multiply connected one. Let us denote this type of transition as a connectivity shift. This transition is similar to a Lifshitz transition, whereby the topology of the Fermi surface changes. However, in contrast to the case of other systems with a two-dimensional Brillouin zone, for instance, bilayer graphene [38,39], in our special case, the Fermi-surface is also a two-dimensional object. As δ is decreased even further to $\delta = 0.0$, the area Ω_0 of the region with $\nu = 1$ reaches a maximum. Let us introduce the ratio r of this area to the total area of the projected Brillouin zone Ω_{BZ} as

$$r = \frac{\Omega_0}{\Omega_{\mathrm{BZ}}}. \tag{6}$$

As expected, due to the bulk boundary correspondence of topological systems, finite winding numbers herald nondispersing zero energy surface states. As one can observe in Figs. 2(f)–2(j), where the spectrum of a slab with finite thickness is depicted, the region corresponding to $\nu = 1$ indeed harbors drumhead surface states. The spatial localization of these states follows from their analogy with the SSH model [33]. Now turning our attention to the parameter ξ and to Fig. 3. we can see that for a fixed value of δ the parameter ξ, which mimics mechanical distortions, can also be used to change the connectivity of the flat portion of the surface-localized zero energy states. As one decreases ξ, a band crossing can be engineered at the Z point, introducing again a second nodal loop, and thus transforming a simply connected disklike region with $\nu = 1$ into an annuluslike region. This thus again leads to a connectivity shift.

C. Interactions

In the previous sections, we showed that the presented model exhibits drumhead surface states. For these states, which occupy a considerable portion of the projected Brillouin zone, the kinetic energy vanishes. Thus, interactions between charge carriers undoubtedly will have a major role in influencing their behavior. The simplest of consequences of interactions might lead to the formation of an ordered magnetic pattern on the surface of the system. This emergent magnetism parallels that of the edge magnetization of zigzag graphene nanoribbons already observed experimentally [40].

We take interactions into account through a Hubbard term and employ a simple mean-field approach to determine the ground state of the system. This simple but pragmatic choice has been successfully employed to characterize two-dimensional semimetals with a flat band. For instance, the magnetic phase diagram of the Lieb lattice was explored by Gouveia and Dias [41]. Temperature and doping-induced instabilities were investigated by Kumar *et al.* [42]. Nematic phases were studied on the dice lattice by Dóra *et al.* [43]. In a joint theoretical and experimental study, the present authors collaborated in an effort to characterize surface states of rhombohedral graphite employing mean-field approaches and beyond mean-field tensor network techniques [31]. It was found that the mean-field approximation yields an appropriate description of the surface state if the system is magnetic.

The full Hamiltonian $\hat{H}$, including the Hubbard term, for the electronic degrees of freedom is cast in the form

$$\hat{H} = \hat{H}_0 + U \sum_i \hat{n}_{i,\uparrow}\hat{n}_{i,\downarrow}, \tag{7}$$

where $\hat{n}_{i,s} = \hat{c}^{\dagger}_{i,s}\hat{c}_{i,s}$ with $\hat{c}_{i,s} = \hat{a}_{\mathbf{r}_i,s}, \hat{b}_{\mathbf{r}_i,s}$. In the present paper, we shall focus on the case of a half-filled system, thus, in all calculations, the Fermi level E_F is set to guarantee

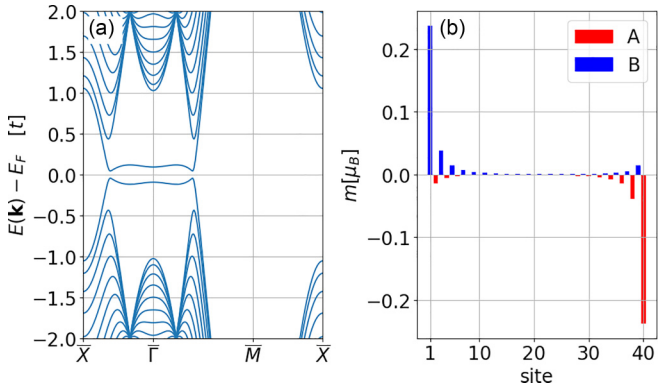

FIG. 4. Self-consistent band structure for both spin species (a) of a slab of $N = 20$ layers after adding the Hubbard term with $U/t = 1.0$ to all sites at $\delta = 3.0$ for an antiferromagnetic alignment of the top and bottom layers. Site magnetization m_i (b) of the many-body ground state obtained after the self-consistent procedure.

this condition. We have to stress here that for magnetism to arise, the system needs to be in the vicinity of half filling, otherwise the spin polarization of the surface states vanishes. This behavior is expected for nodal line semimetals and was already observed in rhombohedral graphene [31]. However, we also note that all mechanisms that make the surface states dispersive, by enhancing its kinetic energy, also will extend the range of the chemical potential at which magnetism can be stabilized.

To further proceed, we analyze the system defined by Eq. (7) on a mean-field level [44]. That is, we obtain an effective spin-dependent single-particle description of the system after a self-consistent procedure. Thus, instead of the interacting Hamiltonian Eq. (7), we work with the mean-field Hamiltonian $\hat{H}_{\text{slab,MF}}(\{n_{i,\uparrow}, n_{i,\downarrow}\})$, which depends explicitly on the self-consistently obtained occupation numbers $n_{i,s}$ at each site. We give further details regarding the applied mean-field method in Appendix B. The results of a mean-field calculation can be observed in Fig. 4(a), where the spectrum of a slab with finite thickness is presented. The impact of interactions is the visible splitting of the zero-energy flat band. The splitting is due to the local difference of the occupation of the two spin species on the surfaces of the system. The magnetization m_i on site i is obtained as

$$m_i = (n_{i,\uparrow} - n_{i,\downarrow})\mu_B, \tag{8}$$

where the occupation numbers $n_{i,s}$ are the expectation value of $\hat{n}_{i,s}$ in the ground state for site i and spin s, while μ_B is the Bohr magneton. Figure 4(b) shows the magnetization for each site in the cross section of a slab of finite thickness. One can observe that the sites on the very top and bottom carry a considerable portion of the overall magnetization. Magnetization drops off exponentially towards the bulk of the system with neighboring layers exhibiting opposite magnetization.

For moderate system thickness where there is still some overlap between the states localized on the two opposing surfaces of the system, an antiferromagnetic configuration is energetically more favorable where the magnetization of the top layer is reversed as compared to that of the bottom layer, as can be observed in Fig. 4(b). In these situations, the ground state of the system possesses an overall spectral gap as can also be seen in Fig. 4(a). For wide enough slabs though, the difference in ground-state energy of the parallel and antiparallel alignment of the magnetization of the opposing surfaces vanishes as the two surfaces effectively decouple from each other.

III. SURFACE MAGNONS

In this section, we are going to analyze the magnetic characteristics of the topmost surface sites of our model. This layer of sites is characterized at zero temperature by an ordered ferromagnetic spin configuration. We start by mapping the localized magnetic moments of the surface, with magnitude m, to that of an isotropic Heisenberg model. The mapping will allow us to find the surface magnon spectrum of the system. From the magnon spectrum, we extract experimentally accessible quantities such as the spin-wave stiffness D and the effective exchange constant $J(\mathbf{0})$. We finish this section by discussing how these quantities depend on the parameters of the model. We shall concentrate on possible observable fingerprints of the connectivity shift discussed in the previous sections.

The classical Heisenberg model describes coupled classical magnetic moments at site i with an orientation $\mathbf{e}_i$ and coupling constants J_{ij} through the classical Hamiltonian:

$$h = -\frac{1}{2}\sum_{i,j} J_{ij}\mathbf{e}_i\mathbf{e}_j. \tag{9}$$

For tight-binding-like electronic systems, with a single spinful orbital on each site, where interactions are taken into account through a Hubbard term with interaction strength U, on the mean-field level, the coupling constants appearing in the above expression can be cast into the rather simple form [45]

$$J_{ij} = \frac{2}{\pi}\left(\frac{mU}{\mu_B}\right)^2 \sum_{i\neq j}\int_{-\infty}^{E_F} dE\ \mathrm{Im}[G^{\uparrow}_{ij}(E)G^{\downarrow}_{ji}(E)]. \tag{10}$$

In this expression, $G^s_{ij}(\varepsilon)$ are the matrix elements of the Green's function $\hat{G}^s(\varepsilon)$ for spin channel s and between surface sites i and j which, in turn, are obtained from the mean-field Hamiltonian $\hat{H}^s_{\text{MF}}$ as

$$\hat{G}^s(E) = \lim_{\eta\to 0}\left((E + i\eta)\hat{I} - \hat{H}^s_{\text{MF}}\right)^{-1}. \tag{11}$$

The Fourier transform of the coupling constants, $J(\mathbf{q})$, can be cast in terms of an integral over the projected Brillouin zone for each wave vector $\mathbf{q}$ as

$$J(\mathbf{q}) = \sum_{j\neq 0} e^{i\mathbf{q}\mathbf{R}_j}J_{0j} = \frac{2}{\pi}\left(\frac{mU}{\mu_B}\right)^2 \mathrm{Im}\int_{-\infty}^{E_F} d\varepsilon\mathcal{I}_{\mathbf{q}}(E), \tag{12}$$

with

$$\mathcal{I}_{\mathbf{q}}(E) = \left(\sum_{\boldsymbol{k}} \mathcal{G}^{\uparrow}_{00}(E,\mathbf{k})\mathcal{G}^{\downarrow}_{00}(E,\mathbf{k}+\mathbf{q})\right) - G^{\uparrow}_{00}(E)G^{\downarrow}_{00}(E). \tag{13}$$

Here $\mathcal{G}^s_{00}(E,\mathbf{k})$ is the surface component of the momentum-dependent Green's function for an infinite slab geometry of finite thickness at momentum $\mathbf{k}$ and spin component s.

As the considered slab system has two-dimensional periodicity, a natural question regarding the stability of long-range magnetic order arises. According to the Mermin-Wagner theorem [46] there is no finite temperature phase transition for systems with continuous symmetry in $d \leqslant 2$ dimensions in the thermodynamic limit. This result has been extended for layered systems as well [47]. However, recently it was pointed out that despite the rigorous limitations regarding the stability of ordered phases in truly infinite systems, realistic device-sized systems may exhibit magnetic ordering [48]. According to Jenkins *et al.*, short-range isotropic interactions can stabilize magnetic order at finite temperatures due to finite-size effects and intrinsic properties of the isotropic exchange coupling. The coupling constants can be used to define a temperature scale, often denoted as the mean-field Curie temperature, as $T_C = J(\mathbf{0})/3k_B$. This crude approximation for the transition temperature can be further refined through Monte Carlo simulations where constituent spins are coupled through the pairwise exchange couplings J_{ij}. We shall use $J(\mathbf{0})$, the effective exchange parameter [49], as a key characteristic property as well.

The dynamics of spin fluctuations are captured by the dispersion relation of magnons, which, in turn, for a ferromagnetic reference state, is given by

$$\varepsilon(\mathbf{q}) = \frac{2\mu_B}{m}(J(\mathbf{0}) - J(\mathbf{q})). \tag{14}$$

This spectrum can be measured, for instance, by spin-polarized electron energy loss spectroscopy [50,51]. For ferromagnetic systems, the curvature D of the magnon spectrum at $\mathbf{q} = \mathbf{0}$ is again an important attribute that is more commonly referred to as spin-wave stiffness, that is,

$$\varepsilon(\mathbf{q})|_{\mathbf{q}\approx\mathbf{0}} = Dq^2. \tag{15}$$

In the following, we present and discuss results for the quantities mentioned above. We put an emphasis on how the energetics of surface magnons are impacted by the two model parameters δ and ξ, particularly around a connectivity shift of the surface flat band. Finite-size scaling shows that as one increases the number of layers N towards the macroscopic limit, the identified signatures of the connectivity shift presented below will manifest precisely at the critical values of parameters, even for weak interaction strengths. For stronger interactions, the fingerprints of the transition will occur already for a moderate number of layers. In the calculations shown, we considered a slab of thickness $N = 20$ layers and an interaction strength of $U/t = 1.0$, which proved to be a pragmatic choice to illustrate our main message. As we did in previous sections, we start our analysis by focusing on the parameter δ and keeping $\xi = 1.0$, that is, we consider a system in the absence of mechanical distortions. The magnon spectrum around a high-symmetry path of the projected Brillouin zone for various values of δ is depicted in Fig. 5. As one can deduce from the graph, reducing the value of δ increases the energy of magnons around the $\overline{\Gamma}$ point. A curious observation can also be made regarding the spectrum for $\delta = 0.0$, namely, that it vanishes not just at $\overline{\Gamma}$ but also at $\overline{M}$. This property, which would point towards the instability of the ferromagnetic phase, in general, can be explained in this particular case. In this instance, the absence of the hopping terms proportional

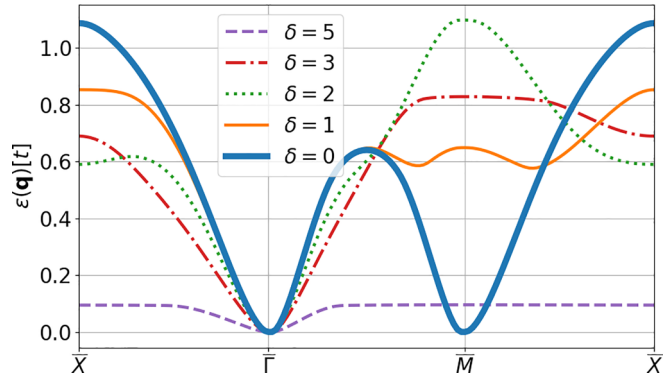

FIG. 5. Surface magnon spectrum of a slab for different values of δ with $\xi = 1.0$.

to δ from the kinetic term $\hat{H}_0$ means that the system falls apart into two interlocked but decoupled subsystems, which can be oriented parallel or antiparallel with respect to each other without any energy cost. To further elucidate important characteristic features of the obtained magnon spectrum, we plot key properties as a function of δ in Fig. 6. We comment first on the evolution of r depicted in Fig. 6(a). As the nodal loop enlarges with decreasing δ, the drum-head surface states occupy more and more area from the projected Brillouin zone. However, decreasing δ beyond the connectivity shift at $\delta = 2.0$, the growth of the ratio r, depicted by an orange dashed line in the figure, suffers a discontinuity. A qualitative observation regarding the connectivity shift can also be made based on the evolution of the magnon energies at the high-symmetry points shown in Fig. 6(b)—a maximum in the vicinity of the connectivity shift at the $\overline{M}$ point while a local minimum at the $\overline{M}$ point is present. Signatures of the connectivity shift are also present in the magnetization m, the effective exchange coupling $J(\mathbf{0})$, and in the stiffness D visualized in Figs. 6(c)–6(e), respectively. Although somewhat hard to discern these directly, they are more readily visible through their derivatives with respect to δ. The derivative of the magnetization $\partial_\delta m$ jumps, the derivative of the effective coupling $\partial_\delta J(\mathbf{0})$ shows a local maximum, while the derivative of the stiffness $\partial_\delta D$ has a local minimum in the vicinity of the connectivity shift at $\delta = 2.0$. In an experimental setting, the parameter δ is typically hard to control, ξ on the other hand is directly linked to a uniaxial distortion of the sample in the z direction. As we discussed previously, a connectivity shift occurs for $\delta = 3.0$ if we decrease ξ below the critical 0.8 value, thus examining the behavior of the above detailed characteristic features for this case as well might highlight experimentally observable fingerprints of this transition. In Fig. 7, the magnon dispersion relation is depicted for distinct values of ξ above, below, and exactly at the connectivity shift. In the panels of Fig. 8, the detailed ξ dependence of the characteristic magnon spectral features is collected. The discontinuity of the evolution of the ratio r at the connectivity shift is evident, as in this case r peaks at the transition point. The magnon energies at the high-symmetry $\overline{M}$ and $\overline{X}$ points as well as the magnetization and the effective exchange coupling show a local maximum in the vicinity of the connectivity shift, while in the evolution of the stiffness a considerable decrease in the slope is observable

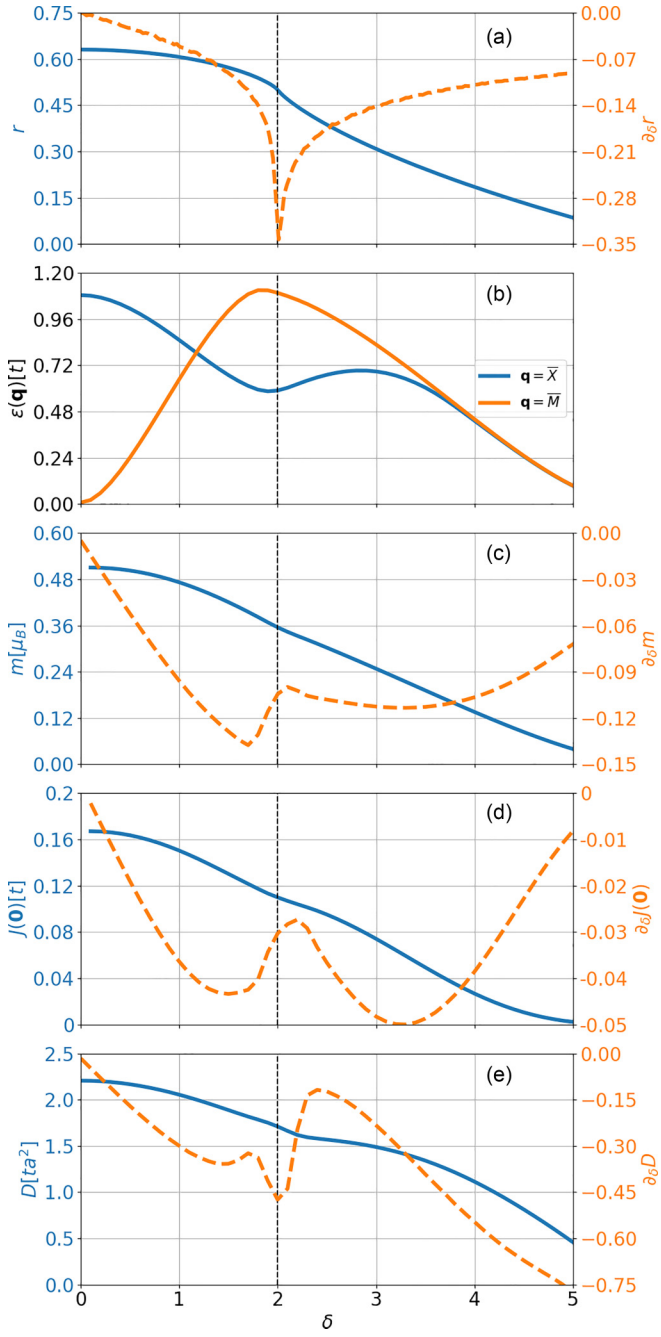

FIG. 6. The ratio r and its derivative with respect to δ (a), the surface magnon spectrum at high symmetry points (b), magnetization m and its derivative (c), effective exchange parameter $J(\mathbf{0})$ with its derivative (d), and stiffness constant D with its derivative (e) for different values of δ at $\xi = 1.0$. A dashed vertical line at $\delta = 2.0$ signals the connectivity shift.

as ξ increases past the transition point. In this case, it will also be insightful to evaluate the derivatives, now with respect to ξ. In all the characteristic properties, there is a clear transition happening at the connectivity shift in the derivatives. The derivatives of m and $J(\mathbf{0})$ both drop sharply while the $\partial_\xi D$ jumps abruptly at the transition point. We note that the oscillations present in this quantity at small ξ values are due to numerical limitations, and as such they should be considered a computational artifact.

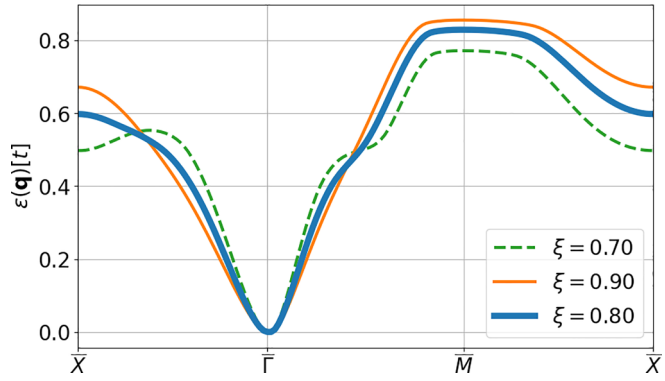

FIG. 7. Surface magnon spectrum of a slab for different values of ξ with $\delta = 3.0$.

IV. ROLE OF SURFACE RECONSTRUCTION

The role of surface reconstruction in a real material can significantly affect the surface-specific properties. Surface termination, especially in the context of thin film or layered materials, can lead to a considerable change in the local Hamiltonian compared to the bulk. In this section, we will explore how surface reconstruction impacts the flatness of the drumhead states and the resulting magnetism.

As a minimal model for surface reconstruction, we include a surface-centered lateral hopping that breaks sublattice symmetry to our slab calculations. We add to the Hamiltonian of the considered slab the following term:

$$H_{\text{surf}} = t' \sum_{\mathbf{r},s,i=(1,2)} \hat{a}^\dagger_{\mathbf{r},s}\hat{a}_{\mathbf{r}+\mathbf{a}_i,s} + \hat{b}^\dagger_{\mathbf{r},s}\hat{b}_{\mathbf{r}+\mathbf{a}_i,s} + \text{H.c.}, \qquad (16)$$

where the summation for the unit cell indices $\mathbf{r}$ run only for those unit cells closest to the surface.

This term has a negligible effect on the bulk states, however, it will have two important consequences regarding the flat surface states. First, the drumhead states will develop finite dispersion; second, the half-filling criterion we used so far will not necessarily keep the Fermi level centered in the flat band.

We illustrate the impact of a finite t' on the flat bands in Fig. 9. In Fig. 9(a), where we compare the single-particle spectrum at $t'/t = 0$ and $t'/t = 0.05$, it is evident that the initially flat surface bands become rippled. Also, now the charge neutrality point denoted by dashed lines is shifted from zero to a finite value. Switching on interactions, as we can observe in Fig. 9(b), can still gap the surface states leading to a magnetized surface. However, as we will discuss below, the half-filling criterion might not favor surface magnetism under all circumstances.

To further clarify the impact of the surface reconstruction parameter t' on the magnetic properties of the surface, we calculated the surface magnetization m, effective exchange parameter $J(\mathbf{0})$, and stiffness constant D as a function of the parameter δ for finite t' values. These characteristic quantities are depicted in Fig. 10. In Fig. 10(a), we show how the surface magnetization evolves for finite surface reconstruction compared to no reconstruction at all. One can observe that for small values of δ, the surface magnetization at half filling closely follows the ideal case of a flat band. However,

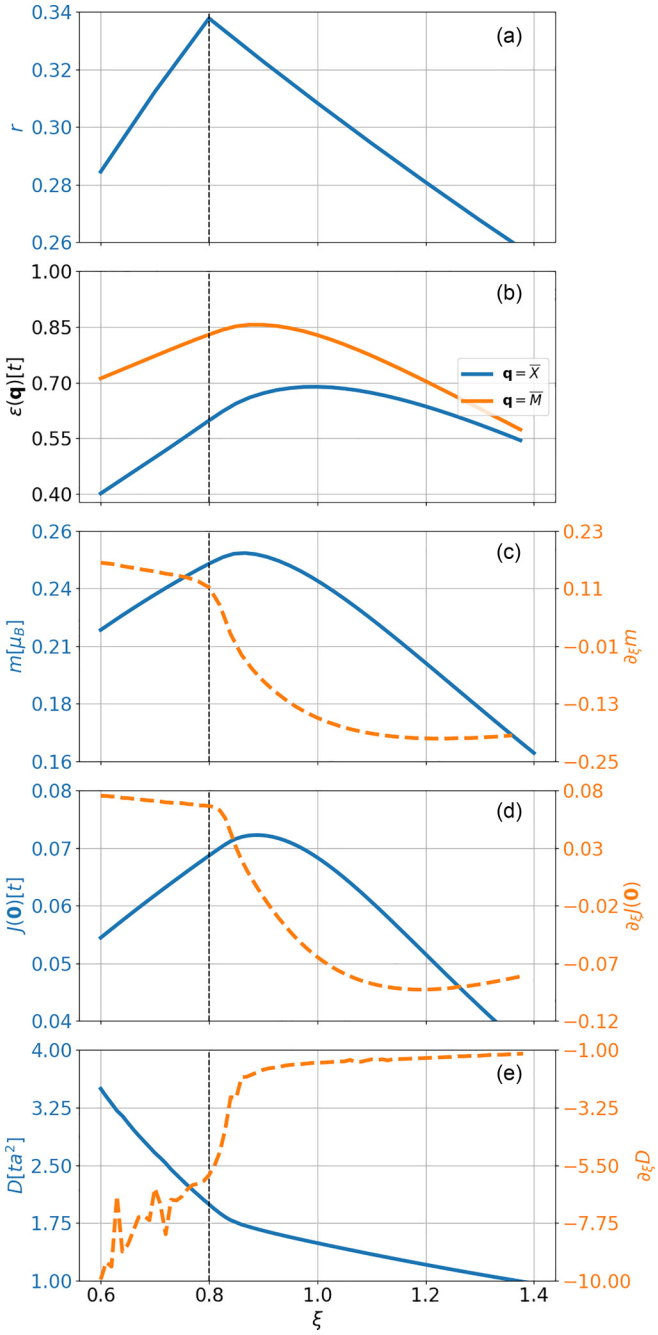

FIG. 8. The ratio r (a), surface magnon spectrum at high symmetry points (b), magnetization m (c), effective exchange parameter $J(\mathbf{0})$, (d) and stiffness constant D (e) for different values of ξ with $\delta = 3.0$. Where appropriate, the right axis shows the scale of the derivative with respect to ξ. The vertical dashed line at $\xi = 0.8$ marks the connectivity shift.

as δ increases, the half-filling criterion sets the Fermi level further from the flat band. As a result, magnetism begins to break down, leading to a nonmagnetic ground state. For $t'/t = 0.05$, the breakdown occurs for $\delta = 3.0$; thus, in this case, the previously detailed effects of the connectivity shift can still be observed. As is evident from the evolution of the effective exchange parameter and the stiffness constant, the distinct signatures of the connectivity shift, especially in the derivative quantities, closely follow the ideal case. We can

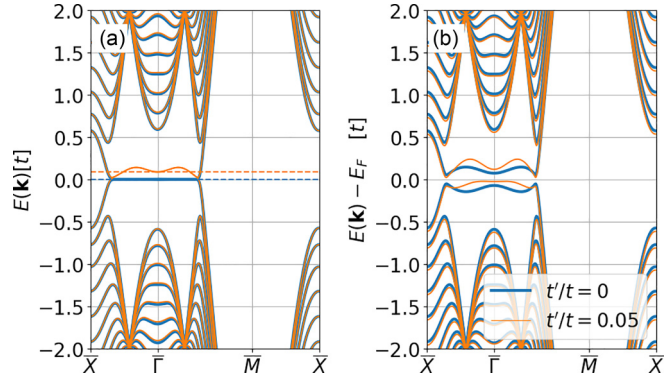

FIG. 9. Single particle spectrum (a) of a slab for $\delta = 2.5$, with and without surface reconstruction t'. Dashed lines denote the energy of half filling. Self-consistent band structure (b) with interaction strength $U/t = 1.0$.

observe a clear peak in $\partial_\delta J(\mathbf{0})$ and a dip in $\partial_\delta D$ at $\delta = 2.0$ for $t'/t = 0.05$.

For larger values of t', the breakdown occurs for smaller values of δ, for instance, in the case of $t'/t = 0.1$ the breakdown already happens before the connectivity shift. However, if we relax the strict half-filling condition and adjust the Fermi level to the center of the flat band, magnetism of the surface can be restored. Experimentally, this can be achieved by applying a back gate voltage to sufficiently thin samples, effectively tuning the electronic filling to a value where magnetism is revived [52].

As we show in this section, surface reconstruction effects indeed play a major role in influencing the magnetic properties of drumhead states in nodal loop semimetals. Based on our results, however, we can state that as long as the chemical potential is appropriately tuned, the effects associated with the connectivity shift remain observable.

V. SUMMARY

In conclusion, we investigated the magnons associated with the drumhead surface states in a simple model of a nodal loop semimetal. The model without interactions exhibits topological flat bands whose shape, and crucially their connectivity, can be controlled by mechanical distortions. Including interactions on a mean-field level, we show that magnetization on the surface is stabilized. Employing a standard Green's function-based technique we obtained the dispersion relation of surface magnons. Determining key, experimentally accessible characteristics of the magnon spectrum, such as the magnetization, the effective exchange coupling, and the spin-wave stiffness, we show that the Lifshitz-like transition of the electronic states can, in principle, be observed through the magnetic properties of the surface.

On the one hand, we emphasize that our presented phenomenological observations would greatly benefit from future analytic calculations which may shed light on the intricate interplay of topology, interactions, and magnetism in this system. On the other hand, our calculations hopefully will encourage experimental exploration of magnetism on the surface of nodal loop semimetals. For instance, Ca_3P_2 [12] with

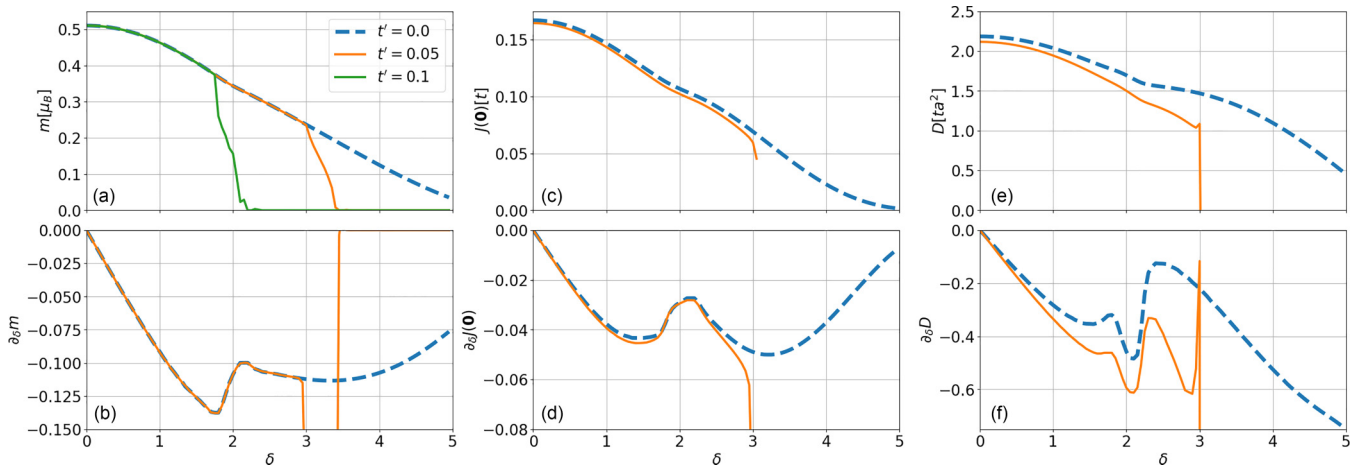

FIG. 10. Characteristic quantities related to magnetism at the surface: (a) magnetization m, (c) effective exchange parameter $J(\mathbf{0})$, and (e) stiffness constant D with the derivatives (b), (d), (f) as a function of the parameter δ calculated with $\xi = 1.0$ for different values of the surface reconstruction parameter t'. The effective exchange parameter and the stiffness constant for the case $t' = 0.05$ is only shown till $\delta = 3.0$, since for larger δ the numerical results become noisy due to the breakdown of surface magnetization.

a relatively large r ratio might be an excellent candidate for future investigations.

ACKNOWLEDGMENTS

The authors express their gratitude to E. McCann, R. Nandkishore, J. Ferrer, A. García Fuente, G. Martinez Carracedo, L. Szunyogh, and L. Udvardi, for valuable discussions and their comments regarding the present paper. This research was supported by the Ministry of Culture and Innovation and the National Research, Development and Innovation Office within the Quantum Information National Laboratory of Hungary (Grant No. 2022-2.1.1-NL-2022-00004) and by NKFIH Grants No. K131938, KKP133827, FK137918, K134437 and K142179. A.A. greatly acknowledges the support from Stipendium Hungaricum No. 249316.

APPENDIX A: APPLICATION OF FOURIER TRANSFORMATION

Below we sketch the steps needed to arrive from Eq. (1) to Eq. (4). Using the inverse relations of the Fourier transform,

$$\hat{a}_{r,s} = \sum_{\mathbf{k}} e^{-i\mathbf{kr}} \hat{a}_{\mathbf{k},s}, \quad \hat{b}_{\mathbf{r},s} = \sum_{\mathbf{k}} e^{-i\mathbf{kr}} \hat{b}_{\mathbf{k},s}, \tag{A1}$$

and the orthogonality criterion of plane waves,

$$\sum_{\mathbf{r}} e^{i(\mathbf{k}-\mathbf{k}')\mathbf{r}} = \delta_{\mathbf{k},\mathbf{k}'}, \tag{A2}$$

the intra unit cell hopping terms are rewritten as

$$\begin{aligned}\sum_{\mathbf{r},s} \hat{a}^\dagger_{\mathbf{r},s}\hat{b}_{\mathbf{r},s} + \text{H.c.} &= \sum_{\mathbf{r},s,\boldsymbol{k}\boldsymbol{k}'} \hat{a}^\dagger_{\mathbf{k},s}\hat{b}_{\mathbf{k}',s} e^{i(\mathbf{k}-\mathbf{k}')\mathbf{r}} + \text{H.c.} \\ &= \sum_{\boldsymbol{k},s} \hat{a}^\dagger_{\mathbf{k},s}\hat{b}_{\mathbf{k},s} + \text{H.c.} \\ &= \sum_{\boldsymbol{k},s} (\hat{a}^\dagger_{\mathbf{k},s}\ \hat{b}^\dagger_{\mathbf{k},s}) \begin{pmatrix} 0 & 1 \\ 1 & 0 \end{pmatrix} \begin{pmatrix} \hat{a}_{\mathbf{k},s} \\ \hat{b}_{\mathbf{k},s} \end{pmatrix} \\ &= \sum_{\boldsymbol{k},s} (\hat{a}^\dagger_{\mathbf{k},s}\ \hat{b}^\dagger_{\mathbf{k},s}) \sigma_x \begin{pmatrix} \hat{a}_{\mathbf{k},s} \\ \hat{b}_{\mathbf{k},s} \end{pmatrix}. \end{aligned} \tag{A3}$$

The inter unit cell hopping terms can be obtained similarly. Along the perpendicular directions, we have

$$\begin{aligned}&\sum_{\mathbf{r},s} \hat{a}^\dagger_{\mathbf{r},s}\hat{b}_{\mathbf{r}+\mathbf{a}_3,s} + \text{H.c.} \\ &= \sum_{\boldsymbol{k},s} (\hat{a}^\dagger_{\mathbf{k},s}\ \hat{b}^\dagger_{\mathbf{k},s}) \begin{pmatrix} 0 & e^{-ik_z} \\ e^{ik_z} & 0 \end{pmatrix} \begin{pmatrix} \hat{a}_{\mathbf{k},s} \\ \hat{b}_{\mathbf{k},s} \end{pmatrix} \\ &= \sum_{\boldsymbol{k},s} (\hat{a}^\dagger_{\mathbf{k},s}\ \hat{b}^\dagger_{\mathbf{k},s}) [\cos(k_x)\sigma_x + \sin(k_z)\sigma_y] \begin{pmatrix} \hat{a}_{\mathbf{k},s} \\ \hat{b}_{\mathbf{k},s} \end{pmatrix}, \end{aligned} \tag{A4}$$

while for the lateral $\mathbf{a}_1$ direction we arrive at

$$\begin{aligned}&\sum_{\mathbf{r},s} \hat{a}^\dagger_{\mathbf{r},s}\hat{b}_{\mathbf{r}+\mathbf{a}_1,s} + \hat{a}^\dagger_{\mathbf{r}+\mathbf{a}_1,s}\hat{b}_{\mathbf{r},s} + \text{H.c.} \\ &= \sum_{\boldsymbol{k},s} (\hat{a}^\dagger_{\mathbf{k},s}\ \hat{b}^\dagger_{\mathbf{k},s}) \begin{pmatrix} 0 & e^{ik_x} + e^{-ik_x} \\ e^{ik_x} + e^{-ik_x} & 0 \end{pmatrix} \begin{pmatrix} \hat{a}_{\mathbf{k},s} \\ \hat{b}_{\mathbf{k},s} \end{pmatrix} \\ &= \sum_{\boldsymbol{k},s} (\hat{a}^\dagger_{\mathbf{k},s}\ \hat{b}^\dagger_{\mathbf{k},s}) 2\cos(k_x)\sigma_x \begin{pmatrix} \hat{a}_{\mathbf{k},s} \\ \hat{b}_{\mathbf{k},s} \end{pmatrix}. \end{aligned} \tag{A5}$$

Combining all terms given by Eq. (1) yields Eq. (4).

APPENDIX B: MEAN-FIELD APPROXIMATION

In this Appendix, we briefly summarize the applied self-consistent procedure used to obtain the mean-field solution. We closely follow the algorithm outlined in Ref. [44]. To obtain the surface magnetization, a slab geometry was considered. To distinguish the planar and perpendicular components of the real-space coordinates $\mathbf{r}$ indexing the electronic degrees of freedom, we introduce in this Appendix the notation $\underline{r}$

for the planar and the label $z = 1 \ldots N$ for the perpendicular component, where N is the number of layers considered. The kinetic term of the slab, based on the bulk expression Eq. (1), can be cast as

$$\begin{aligned}\hat{H}_{\text{slab},0} = \sum_{\underline{r},s} \Bigg(& \sum_{z=1}^{N} \delta\xi t \hat{a}^{\dagger}_{\underline{r},z,s} \hat{b}_{\underline{r},z,s} - \sum_{z=1}^{N-1} 2\xi t \hat{a}^{\dagger}_{\underline{r},z,s} \hat{b}_{\underline{r},z+1,s} \\ & - t \sum_{z=1}^{N} [\hat{a}^{\dagger}_{\underline{r}+\underline{a}_1,z,s} \hat{b}_{\underline{r},z,s} + \hat{a}^{\dagger}_{\underline{r},z,s} \hat{b}_{\underline{r}+\underline{a}_1,z,s}] \\ & - t \sum_{z=1}^{N} [\hat{a}^{\dagger}_{\underline{r}+\underline{a}_2,z,s} \hat{b}_{\underline{r},z,s} + \hat{a}^{\dagger}_{\underline{r},z,s} \hat{b}_{\underline{r}+\underline{a}_2,z,s}] \Bigg) + \text{H.c.},\end{aligned} \tag{B1}$$

where $\hat{a}_{\underline{r},z,s}$ ($\hat{b}_{\underline{r},z,s}$) is the annihilation operator of elections on sublattice A (B), at the lateral position $\underline{r}$, layer z and spin s. We also introduce two-dimensional lateral lattice vectors $\underline{a}_{1,2}$ having the same lateral components as $\mathbf{a}_{1,2}$. Exploiting the two-dimensional periodicity of the slab geometry, we can recast the above expression in terms of the two-dimensional wave number $\underline{k}$ as

$$\hat{H}_{\text{slab},0} = \sum_{\underline{k},s} \hat{c}^{\dagger}_{\underline{k},s} \mathcal{H}_{\text{slab},0}(\underline{k}) \hat{c}_{\underline{k},s}, \tag{B2}$$

with the Fourier-transformed operators

$$\hat{a}_{\underline{k},z,s} = \sum_{\underline{r}} e^{\mathrm{i}\underline{k}\underline{r}} \hat{a}_{\underline{r},z,s}, \quad \hat{b}_{\underline{k},z,s} = \sum_{\underline{r}} e^{\mathrm{i}\underline{k}\underline{r}} \hat{b}_{\underline{r},z,s} \tag{B3}$$

and compound operator $\hat{c}_{\underline{r},z,s}$ defined as

$$\hat{c}^{\dagger}_{\underline{k},s} = (\hat{a}^{\dagger}_{\underline{k},1,s} \quad \hat{b}^{\dagger}_{\underline{k},1,s} \quad \ldots \quad \hat{a}^{\dagger}_{\underline{k},N,s} \quad \hat{b}^{\dagger}_{\underline{k},N,s}). \tag{B4}$$

Introducing the abbreviations

$$\Delta = \delta\xi t - 2t\cos(k_x) - 2t\cos(k_y), \quad \Xi = -2\xi t, \tag{B5}$$

the $2N \times 2N$ coefficient matrix $\mathcal{H}_{\text{slab},0}(\underline{k})$ is cast in the simple form

$$\mathcal{H}_{\text{slab},0}(\underline{k}) = \begin{pmatrix} 0 & \Delta & 0 & 0 & & & \\ \Delta & 0 & \Xi & 0 & & & \\ 0 & \Xi & 0 & \Delta & & & \\ 0 & 0 & \Delta & 0 & \ddots & 0 & 0 \\ & & & \ddots & \ddots & \Xi & 0 \\ & & & 0 & \Xi & 0 & \Delta \\ & & & 0 & 0 & \Delta & 0 \end{pmatrix}, \tag{B6}$$

which highlights, for a given $\underline{k}$, the similarity of the considered model to the SSH chain.

We take interactions into account through a Hubbard term by considering the Hamiltonian

$$\hat{H}_{\text{slab}} = \hat{H}_{\text{slab},0} + U \sum_{\underline{r},z} \hat{n}_{\underline{r},z,\uparrow} \hat{n}_{\underline{r},z,\downarrow}, \tag{B7}$$

with occupation number operators $\hat{n}_{\underline{r},z,s}$ acting on the appropriate degrees of freedom. Applying a mean-field approximation gives us a self-consistent equation for the expectation values $n_{z,s}$ of the occupations for the degrees of freedom in the unit cell of the slab. In this paper, we always consider half filling. Each unit cell of the slab contains N layers with two sublattices and two spin components, that is, a total of $4N$ degrees of freedom. Thus, the occupations are restricted to obey the relation $\sum_{z,s} n_{z,s} = 2N$. The mean-field Hamiltonian is an effective noninteracting operator

$$\hat{H}_{\text{slab,MF}} = \sum_{\underline{k},s} \hat{c}^{\dagger}_{\underline{k},s} \mathcal{H}_{\text{slab},s}(\underline{k}) \hat{c}_{\underline{k},s}, \tag{B8}$$

where we introduce the spin-dependent $\mathcal{H}_{\text{slab},s}$ matrices as

$$\begin{aligned}\mathcal{H}_{\text{slab},\uparrow}(k) &= \mathcal{H}_{\text{slab},0}(k) + U\mathcal{D}_{\downarrow}, \\ \mathcal{H}_{\text{slab},\downarrow}(k) &= \mathcal{H}_{\text{slab},0}(k) + U\mathcal{D}_{\uparrow},\end{aligned} \tag{B9}$$

where $\mathcal{D}_s$ is a diagonal matrix containing the occupations $n_{z,s}$ of spin projection s. Obtaining the eigenvalues $E_l(\underline{k}, s)$ and eigenvectors $\phi_l(\underline{k}, z, s)$ of the coupled equations above allows us to close the self-consistency loop by expressing the occupation numbers $n_{z,s}$ as

$$n_{z,s} = \sum_{\substack{l,\underline{k} \\ E_l(\underline{k},s) < E_{\text{F}}}} |\phi_l(\underline{k}, z, s)|^2, \tag{B10}$$

where the Fermi energy E_{F} is determined to enforce the half-filling condition.

[1] M. Z. Hasan and C. L. Kane, Rev. Mod. Phys. **82**, 3045 (2010).
[2] X.-L. Qi and S.-C. Zhang, Rev. Mod. Phys. **83**, 1057 (2011).
[3] C. Fang, H. Weng, X. Dai, and Z. Fang, Chin. Phys. B **25**, 117106 (2016).
[4] B. Yan and C. Felser, Annu. Rev. Condens. Matter Phys. **8**, 337 (2017).
[5] N. P. Armitage, E. J. Mele, and A. Vishwanath, Rev. Mod. Phys. **90**, 015001 (2018).
[6] S.-Y. Yang, H. Yang, E. Derunova, S. S. Parkin, B. Yan, and M. N. Ali, Adv. Phys.: X **3**, 1414631 (2018).
[7] X. Wan, A. M. Turner, A. Vishwanath, and S. Y. Savrasov, Phys. Rev. B **83**, 205101 (2011).
[8] A. A. Burkov and L. Balents, Phys. Rev. Lett. **107**, 127205 (2011).
[9] B. Q. Lv, H. M. Weng, B. B. Fu, X. P. Wang, H. Miao, J. Ma, P. Richard, X. C. Huang, L. X. Zhao, G. F. Chen, Z. Fang, X. Dai, T. Qian, and H. Ding, Phys. Rev. X **5**, 031013 (2015).

[10] C. Fang, Y. Chen, H.-Y. Kee, and L. Fu, Phys. Rev. B **92**, 081201(R) (2015).

[11] R. Yu, H. Weng, Z. Fang, X. Dai, and X. Hu, Phys. Rev. Lett. **115**, 036807 (2015).

[12] L. S. Xie, L. M. Schoop, E. M. Seibel, Q. D. Gibson, W. Xie, and R. J. Cava, APL Mater. **3**, 083602 (2015).

[13] J.-L. Lu, W. Luo, X.-Y. Li, S.-Q. Yang, J.-X. Cao, X.-G. Gong, and H.-J. Xiang, Chin. Phys. Lett. **34**, 057302 (2017).

[14] R. Bi, Z. Yan, L. Lu, and Z. Wang, Phys. Rev. B **96**, 201305(R) (2017).

[15] S. Zhu and S. Syzranov, Ann. Phys. **459**, 169501 (2023).

[16] J. S. Silva, M. A. N. Araújo, M. Gonçalves, P. Ribeiro, and E. V. Castro, Phys. Rev. B **107**, 045146 (2023).

[17] L. Li, J. Cao, C. Cui, Z.-M. Yu, and Y. Yao, Phys. Rev. B **108**, 085120 (2023).

[18] Y. Wang, T. Bömerich, J. Park, H. F. Legg, A. A. Taskin, A. Rosch, and Y. Ando, Phys. Rev. Lett. **131**, 146602 (2023).

[19] C. Song, L. Liu, S. Cui, J. Gao, P. Song, L. Jin, W. Zhao, Z. Sun, X. Zhang, L. Zhao, X. Luo, Y. Sun, Y. Shi, H. Zhang, G. Liu, and X. J. Zhou, Phys. Rev. B **107**, 045142 (2023).

[20] M. Hosoi, I. Tateishi, H. Matsuura, and M. Ogata, Phys. Rev. B **105**, 085406 (2022).

[21] M. Takeichi, R. Furuta, and S. Murakami, Phys. Rev. B **107**, 085139 (2023).

[22] M. N. Baibich, J. M. Broto, A. Fert, F. Nguyen Van Dau, F. Petroff, P. Etienne, G. Creuzet, A. Friederich, and J. Chazelas, Phys. Rev. Lett. **61**, 2472 (1988).

[23] S. D. Bader and S. Parkin, Annu. Rev. Condens. Matter Phys. **1**, 71 (2010).

[24] Y. Tokura, K. Yasuda, and A. Tsukazaki, Nat. Rev. Phys. **1**, 126 (2019).

[25] R. Nandkishore, Phys. Rev. B **93**, 020506(R) (2016).

[26] Y. Wang and R. M. Nandkishore, Phys. Rev. B **95**, 060506(R) (2017).

[27] B. Roy, Phys. Rev. B **96**, 041113 (2017).

[28] M. Campetella, J. Baima, N. M. Nguyen, L. Maschio, F. Mauri, and M. Calandra, Phys. Rev. B **101**, 165437 (2020).

[29] J. H. Muten, A. J. Copeland, and E. McCann, Phys. Rev. B **104**, 035404 (2021).

[30] H. Zhou, T. Xie, A. Ghazaryan, T. Holder, J. R. Ehrets, E. M. Spanton, T. Taniguchi, K. Watanabe, E. Berg, M. Serbyn *et al.*, Nature (London) **598**, 429 (2021).

[31] I. Hagymási, M. S. Mohd Isa, Z. Tajkov, K. Márity, L. Oroszlány, J. Koltai, A. Alassaf, P. Kun, K. Kandrai, A. Pálinkás *et al.*, Sci. Adv. **8**, eabo6879 (2022).

[32] Y.-H. Chan, C.-K. Chiu, M. Y. Chou, and A. P. Schnyder, Phys. Rev. B **93**, 205132 (2016).

[33] W.-P. Su, J. R. Schrieffer, and A. J. Heeger, Phys. Rev. Lett. **42**, 1698 (1979).

[34] M. Hirayama, R. Okugawa, T. Miyake, and S. Murakami, Nat. Commun. **8**, 14022 (2017).

[35] S. Ryu and Y. Hatsugai, Phys. Rev. Lett. **89**, 077002 (2002).

[36] M.-X. Yang, W. Luo, and W. Chen, Adv. Phys.: X **7**, 2065216 (2022).

[37] J. K. Asbóth, L. Oroszlány, and A. Pályi, Lect. Notes Phys. **919**, 166 (2016).

[38] Y. Lemonik, I. Aleiner, C. Toke, and V. Fal'ko, Phys. Rev. B **82**, 201408(R) (2010).

[39] A. Varlet, D. Bischoff, P. Simonet, K. Watanabe, T. Taniguchi, T. Ihn, K. Ensslin, M. Mucha-Kruczyński, and V. I. Fal'ko, Phys. Rev. Lett. **113**, 116602 (2014).

[40] G. Z. Magda, X. Jin, I. Hagymási, P. Vancsó, Z. Osváth, P. Nemes-Incze, C. Hwang, L. P. Biro, and L. Tapasztó, Nature (London) **514**, 608 (2014).

[41] J. Gouveia and R. Dias, J. Magn. Magn. Mater. **382**, 312 (2015).

[42] P. Kumar, T. I. Vanhala, and P. Törmä, Phys. Rev. B **96**, 245127 (2017).

[43] B. Dóra, I. F. Herbut, and R. Moessner, Phys. Rev. B **90**, 045310 (2014).

[44] Y. Claveau, B. Arnaud, and S. Di Matteo, Eur. J. Phys. **35**, 035023 (2014).

[45] L. Oroszlány, J. Ferrer, A. Deák, L. Udvardi, and L. Szunyogh, Phys. Rev. B **99**, 224412 (2019).

[46] N. D. Mermin and H. Wagner, Phys. Rev. Lett. **17**, 1133 (1966).

[47] A. Gelfert and W. Nolting, J. Phys.: Condens. Matter **13**, R505 (2001).

[48] S. Jenkins, L. Rózsa, U. Atxitia, R. F. Evans, K. S. Novoselov, and E. J. Santos, Nat. Commun. **13**, 6917 (2022).

[49] A. I. Liechtenstein, M. Katsnelson, V. Antropov, and V. Gubanov, J. Magn. Magn. Mater. **67**, 65 (1987).

[50] K. Zakeri, Y. Zhang, and J. Kirschner, J. Electron Spectrosc. Relat. Phenom. **189**, 157 (2013).

[51] K. Zakeri, H. Qin, and A. Ernst, Commun. Phys. **4**, 18 (2021).

[52] K. Myhro, S. Che, Y. Shi, Y. Lee, K. Thilahar, K. Bleich, D. Smirnov, and C. Lau, 2D Mater. **5**, 045013 (2018).